

Canted Antiferromagnetism in the Quasi-1D Iron Chalcogenide BaFe_2Se_4

Xiaoyuan Liu,¹ Keith M. Taddei,² Sheng Li,¹ Wenhao Liu,¹ Nikhil Dhale,¹

Rashad Kadado,¹ Diana Berman,³ Clarina Dela Cruz,² and Bing Lv^{1,4,*}

¹*Department of Physics, University of Texas at Dallas, Richardson, Texas 75080, USA*

²*Neutron Scattering Division, Oak Ridge National Laboratory, Oak Ridge, Tennessee 37831, USA*

³*Department of Materials Science and Engineering,*

University of North Texas, Denton, Texas 76203, USA

⁴*Department of Materials Science and Engineering,*

University of Texas at Dallas, Richardson, Texas 75080, USA

We report the synthesis and physical properties studies of quasi-1D iron chalcogenide BaFe_2Se_4 which shares the FeSe_4 tetrahedra building motif commonly seen in the iron chalcogenide superconductors. A high-quality polycrystalline sample was achieved by solid-state reaction method and characterized by X-ray diffraction, electrical resistivity, magnetic susceptibility and neutron diffraction measurements. BaFe_2Se_4 is a narrow gap semiconductor that magnetically orders at ~ 310 K. Both neutron powder diffraction results and isothermal M - H loops suggest a canted antiferromagnetic structure where Fe sublattice are antiferromagnetically ordered along the c -axis quasi-1D chain direction, resulting in a net ferromagnetic moment in the perpendicular direction along the a -axis with tilted angle of 18.7° towards the b -axis.

The discovery of iron-based superconductors^{1,2} has significantly changed the landscape of unconventional superconductivity in the past decade. Among all the iron-based superconductors, two major chalcogenide-based families have been intensively studied. First, the FeSe , with the simplest crystal structure and bulk superconductivity at 8 K at ambient pressure^{3,4} and at 37 K under high pressure⁵⁻⁹, has caught particular research interest in the past few years due to the significantly enhanced interfacial superconductivity with T_c up to 65 K found in the epitaxial single-layer $\text{FeSe}/\text{SrTiO}_3$ system¹⁰⁻¹⁵. The second major family is alkali metal ($\text{A} = \text{K}, \text{Rb}, \text{Cs}, \text{and Tl}$) intercalated $\text{A}_{1-x}\text{Fe}_{2-y}\text{Se}_2$ superconductors with $T_c \sim 30$ K¹⁶⁻²² where the interplay of vacancy order, magnetism, orbital-selective Mott phase, and superconductivity have been intensively studied²²⁻²⁶. New chemical intercalation routes²⁷⁻³³ also results in several new superconductors with higher T_c such as the $\text{Li}_x(\text{NH}_2)_y(\text{NH}_3)_{1-y}\text{Fe}_2\text{Se}_2$ ($x \sim 0.6$; $y \sim 0.2$), and $(\text{Li}, \text{Fe})\text{OHFeSe}$. Nevertheless, the essential charge carrier layers of these chalcogenide superconductors, two-dimensional (2D) Fe_2Se_2 square lattice formed by the edge-sharing FeSe_4 tetrahedra, are the fundamental building block of all the Fe-based superconductors.

The spin-ladder compound BaFe_2Se_3 is structurally related to the iron chalcogenide superconductors mentioned above, but with a reduced dimensionality. The structure consists of the same building motif, edge-sharing FeSe_4 tetrahedra, but stacked along the b -axis thus forming unique quasi-one-dimensional (quasi-1D) double chains of $[\text{Fe}_2\text{Se}_3]$ instead of the 2D $[\text{Fe}_2\text{Se}_2]$ lattice seen in the iron chalcogenide superconductors. It exhibits unique spin-ladder magnetic structure and long-range-ordered antiferromagnetic order below $T_N \sim 250$ K, and short-range magnetic correlations at room temperature^{34,35}. The antiferromagnetism changes from block-type in BaFe_2Se_3 to stripe-type in BaFe_2S_3 , KFe_2Se_3 , and CsFe_2Se_3 ³⁶⁻³⁸. Interestingly, superconductivity has

been reported in both BaFe_2Se_3 and BaFe_2S_3 compounds under high pressure, with $T_c \sim 11$ K³⁹ above 10 GPa for BaFe_2Se_3 , and $T_c \sim 24$ K above 10 GPa for BaFe_2S_3 ⁴⁰, respectively. They are the only reported materials so far to exhibit a superconducting phase under pressure in this spin-ladder family. This is rather intriguing as the superconductivity in BaFe_2Se_3 emerges near a possible orbital-selective Mott-insulator³⁹, which might provide additional insight into the understanding of the 2D iron chalcogenide superconductors.

BaFe_2Se_4 is another new quasi-1D iron chalcogenide based on the FeSe_4 tetrahedra building motif but with a simpler and different structure from that of the BaFe_2Se_3 compound. The difference between the two crystal structures of BaFe_2Se_4 and BaFe_2Se_3 is shown in Figure 1a. Unlike the spin-ladder double chains in the BaFe_2Se_3 , the quasi-1D chain in the BaFe_2Se_4 consists only of single chains of edge-sharing FeSe_4 tetrahedra along the c -axis separated by Ba atoms. Figure 1b and Figure 1c are highlighting the quasi-1D chain along different directions. The interlayer chains are well separated from each other, with a Fe-Fe distance between the interlayer neighboring 1D Fe chains of $5.663(1)$ Å and the closest Se-Se distance of $3.489(8)$ Å. On the other hand, within the quasi-1D chain (Figure 1c), the Fe-Fe interchain distance is $2.742(9)$ Å and the Fe-Se distance within the FeSe_4 tetrahedra is $2.349(5)$ Å. Both are pretty comparable with the distances in the BaFe_2Se_3 and other iron chalcogenide superconductors.

However, to date, only the structural determination based on small grains (~ 50 μm) has been reported for this compound⁴¹. Previous synthesis attempts from pure elements and repeated regrinding/annealing using different temperature profiles up to 1100°C do not yield an X-ray powder pure phase⁴¹. Therefore, no systematic transport and magnetic characterizations have been carried out on this compound. Band structure calculations, on the other hand, suggest the Fermi level of this com-

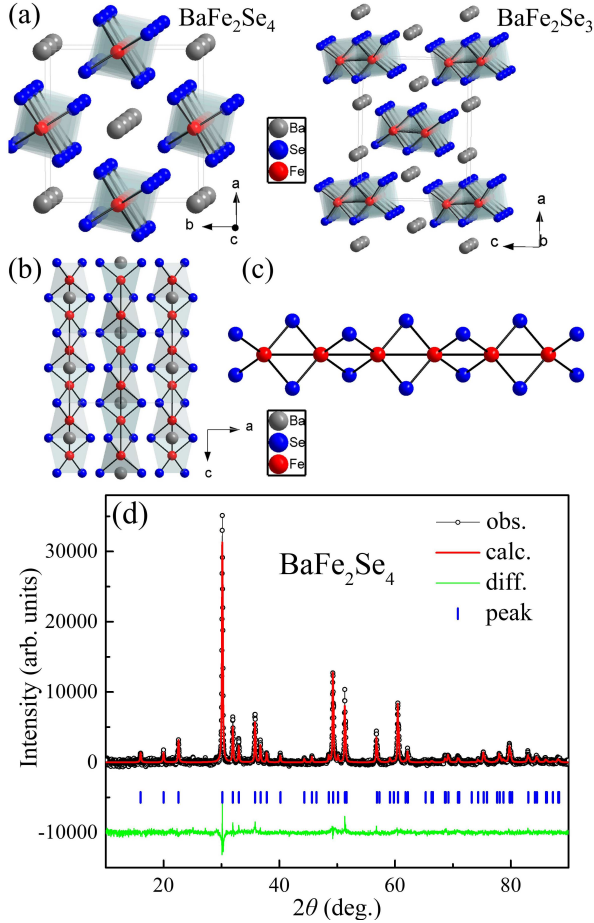


FIG. 1: (a) Schematic crystal structure of BaFe₂Se₄ and BaFe₂Se₃. Both compounds adopt similar quasi-1D structure consist of edge-sharing FeSe₄ tetrahedra, forming single chains in BaFe₂Se₄ while double chains in BaFe₂Se₃ (b) the view from the *b*-axis for BaFe₂Se₄ (c) The detailed microstructure of infinite chains of edge-sharing FeSe₄ tetrahedra along the *c*-axis for BaFe₂Se₄. (d) X-ray diffraction pattern and Rietveld refinement results of the BaFe₂Se₄ at room temperature. The black circles are experimental data, the red curve is the Rietveld refinement fit, and the green curve is the difference. The tick marks indicate the allowed Bragg reflections.

TABLE I: Refined atomic position at room temperature from Rietveld analysis for BaFe₂Se₄ in the $I4_1/m$ space group with $a = 8.0150(1)$ Å, and $c = 5.4936(2)$ Å. U_{eq} is defined as one-third of the trace of the orthogonalized U_{ij} tensor.

Atom	Wyck.	x	y	z	$U_{eq}(\text{\AA}^2)$
Ba	2b	1/2	1/2	0	0.0411(6)
Se	8h	0.70360(6)	0.12350(6)	0	0.0195(3)
Fe	4d	1/2	0	1/4	0.0167(6)

pound lies near a local minimum in the density of states and an overall metallic behavior for BaFe₂Se₄⁴¹. In this work, we present our studies on high quality and X-ray pure phase BaFe₂Se₄ polycrystalline samples. In con-

trast to the previous calculation results, we show that the compound is actually semiconducting with an excitation energy of ~ 142 meV. More importantly, it contains a unique magnetic transition at ~ 310 K caused by canted antiferromagnetic interactions between the neighboring Fe-Fe atoms based on magnetic susceptibility and neutron diffraction studies.

The BaFe₂Se₄ polycrystalline sample was synthesized by the solid-state reaction method using elemental Ba pieces (Alfa Aesar, 99+%), Fe granules (Alfa Aesar, 99.98%) and Se shots (Alfa Aesar, 99.999%). The reaction was carried out at 700 °C in the sealed quartz tube for 2 days, followed by slowly cooling down to room temperature in 10 hours. In particular, two strategies have been utilized during the synthesis to ensure the high-quality powder synthesis and to avoid the formation of small yet magnetic FeSe₂, Fe₇Se₈, Fe_{1-x}Se and other Fe related impurities phases as commonly seen in the previous reports and other ternary iron chalcogenide phases: (1) an excess of $\sim 5\%$ Se was used to compensate the Se lost during the initial reaction from elements. (2) after the initial reaction, small representative sample is scanned by X-ray diffraction (XRD) for initial screening of phase purity where a small amount of FeSe ($< 5\%$ based on XRD analysis) is detected. To further remove this impurity and potentially other amorphous impurities that could not be detected by XRD, a precise amount of BaSe₃ corresponding to that needed to facilitate the reaction of BaSe₃ + FeSe \rightarrow BaFe₂Se₄ is added to the bulk powder, and is reground together with the samples. The assembly is pelletized and annealed at slightly lower temperature 600 °C for 2 weeks. To further improve homogeneity and quality of the samples, several cycles (> 2 times) of regrinding and longtime annealing (> 2 weeks) at 600 °C are also carried out. A typical run of the sample normally takes more than 6 weeks to be finished. Such prolonged annealing time also exclude the formation of amorphous impurities as well. The obtained BaFe₂Se₄ sample is stable in air, and we do not observe any impurity peaks based on XRD analysis and magnetic susceptibilities measurement.

The powder sample was characterized at room temperature by XRD using a Rigaku Smartlab diffractometer and the Rietveld refinements were carried out using FULLPROF and GSAS software packages^{42,43}. The XRD pattern of the synthesized BaFe₂Se₄ sample and corresponding structural refinement results are presented in Figure 1d and Table I. Based on the Rietveld analysis, the synthesized BaFe₂Se₄ sample crystallizes in the tetragonal space group $I4_1/m$ (87) with $a = b = 8.0150(1)$ Å, and $c = 5.4936(2)$ Å, consistent with the values reported in early literature⁴¹. All diffraction peaks for BaFe₂Se₄ can be well indexed and no impurities are detected within XRD resolution. Together with the good refinement values $R = 1.71\%$ and $R_{wp} = 2.52\%$, this suggests high quality of our synthesized BaFe₂Se₄ powder sample.

The electrical transport was measured with Quantum

Design PPMS, using the standard four-probe method. The temperature dependent electrical resistivity data are shown in Figure 2. The resistivity shows an overall semi-conducting behavior, which is in contradiction with previous band structure calculations⁴¹, but in agreement with the measurement reported for its isostructural counterpart BaFe_2S_4 ⁴⁴. We note that the resistivity value at room temperature is $35.5 \, \Omega \, \text{cm}$, which is slightly larger than that of spin-ladder compound BaFe_2Se_3 ($17 \, \Omega \, \text{cm}$)⁴⁵. The resistivity can be fit quite well using thermal activation model $\rho = \rho_0 \exp(\Delta/k_B T)$, where ρ_0 is a prefactor, and k_B is the Boltzmann constant. The inset of Figure 2 shows the results of linear fitting of $\ln(\rho)$ vs. $1/T$, which is consistent with the standard activation model. The activation energy estimated from the fitting is $\Delta = 142.5 \, \text{meV}$, which is comparable to the reported gap value of BaFe_2Se_3 ($\sim 180 \, \text{meV}$)⁴⁵.

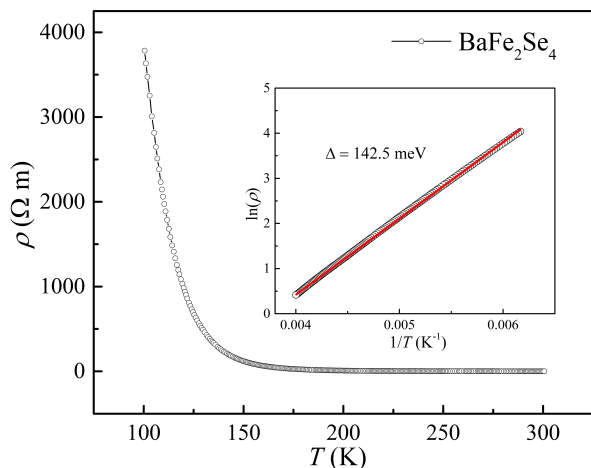


FIG. 2: Temperature dependence of resistivity on BaFe_2Se_4 and the inset shows fitting results from $\ln(\rho)$ vs. $1/T$.

The dc magnetic susceptibility and field-dependent magnetization were measured with Quantum Design MPMS down to 5 K and up to 5 T. The temperature dependence of the magnetization of BaFe_2Se_4 from 5 K to 350 K under different magnetic fields is presented in Figure 3a. A spontaneous magnetization appears at $\sim 310 \, \text{K}$ and increases monotonically below this transition with decreasing temperature. Together with the clear splitting of magnetization between the zero-field-cooled (ZFC) and field-cooled (FC) mode, this indicates the existence of a ferromagnetic component below the transition temperature. The M_{ZFC} and M_{FC} splitting becomes weaker with an increasing magnetic field eventually nearly overlapping at 1 T. The magnetization starts to saturate to a nearly constant plateau below about 50 K. Increasing the applied magnetic field increases the absolute value of the magnetization, but the change of transition temperature T_c is rather small ($< 5 \, \text{K}$). The exact transition temperature is tracked best in the temperature derivative of the normalized magnetization dM/HdT , depicted in inset of Figure 3a. No traceable magnetic transition at \sim

120 K from Fe-Se binary phase (Fe_7Se_8) is observed, further suggesting the success of our synthetic approach for high-quality samples. A small blip at $\sim 50 \, \text{K}$ in ZFC data at 1 T was observed which is due to some trapped oxygen in the powder samples, which is non-intrinsic signal of BaFe_2Se_4 sample. To obtain the effective magnetic moment of Fe in BaFe_2Se_4 , we performed Curie-Weiss fitting over the high-temperature range. To eliminate the influence of ferromagnetic behavior, the temperature range between 330 K and 350 K was chosen at where the $M(T)/H$ curves of 100 Oe, 1000 Oe, and 1 T overlap with each other. The susceptibility does follow the Curie-Weiss law $\chi = C/(T - \theta)$ quite nicely, with Curie constant $C = 2.82 \, \text{emu K/mol}$ and Curie temperature $\theta = 329 \, \text{K}$. The resulting Curie constant corresponds to an effective magnetic moment of $\mu_{\text{eff}} = 3.36 \, \mu_B/\text{Fe}$ ($4.75 \, \mu_B/\text{f.u.}$). The positive θ , which is close to the transition temperature, on the other hand, indicates ferromagnetic interactions in the samples.

The field dependence measurements of the magnetization for BaFe_2Se_4 from -5 T to 5 T at different temperatures from 20 K to 350 K were carried out to further explore the nature of magnetic orders and are shown in Figure 3b. A weak yet clear magnetic hysteresis has been observed below 310 K, however the magnetization did not saturate at a high magnetic field, instead, linear dependent M - H curves suggest an antiferromagnetic state is observed. The magnetic hysteresis loop is suppressed with increasing temperature and eventually disappears and becomes a straight line by 350 K. No hysteresis nor clear remnant signal is observed in the isothermal M - H loop at 350 K, suggesting the ferromagnetic components are not due to amorphous iron or iron oxide impurities, which all have a Curie temperature above 450 K. This further suggests that the observed concurrence of the ferromagnetic and antiferromagnetic state is an intrinsic property of our samples. For a high-quality pure phase, this M - H behavior is consistent with the canted antiferromagnetic state in the BaFe_2Se_4 system in which the ferromagnetic order is provided by the small component canted by magnetic moment of Fe.

The hysteresis loop at 20 K closes up at the field value $H \sim 2.6 \, \text{T}$ and shows a coercive field of $H_c = 5.6 \, \text{kOe}$. The linear antiferromagnetic behavior appears hold up to 5 T, the highest field we have measured. To extract the saturation moment caused by the ferromagnetic component, the $M(H)$ curve at the high field was fit using $M(H) = M_S + M_{\text{AFM}}$, where M_S is the saturation moment which is field independent at the high magnetic field and M_{AFM} is the antiferromagnetic contribution which has a linear relationship to the magnetic field. Through this fitting, we are able to subtract the linear contribution $\chi_{\text{AFM}}H$ from the experimental data, as shown in the inset of Figure 3b. The moment of the ferromagnetic component could also be extracted from the saturated magnetization, from which we obtained $\sim 0.013 \, \mu_B/\text{Fe}$. This value is way smaller than the effective moment calculated by Curie-Weiss law, which further supports the

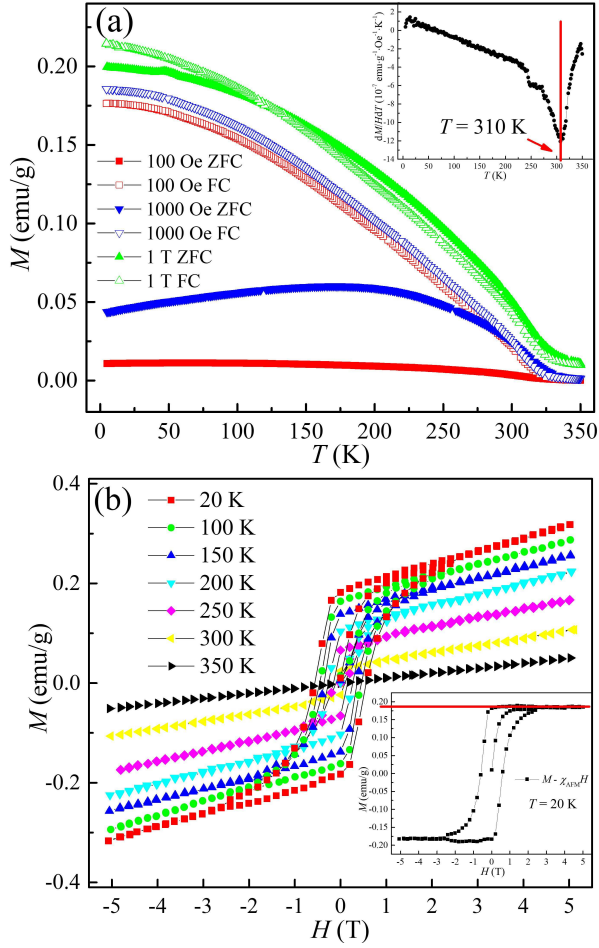


FIG. 3: (a) Magnetization as a function of temperature $M(T)$ of BaFe_2Se_4 measured with ZFC and FC modes at different applied magnetic fields. The inset shows the transition temperature determined from the dM/dT vs. T plot. (b) Magnetization as a function of field $M(H)$ of BaFe_2Se_4 measured at different temperatures from 20 K to 350 K. The magnetic hysteresis loop is suppressed with increasing temperature and eventually disappears and becomes a straight line when temperature reaches 350 K. The inset shows the fitting data after subtracting the linear antiferromagnetic contribution $\chi_{\text{AFM}}H$ at 20 K.

canted antiferromagnetism scenario in BaFe_2Se_4 .

In order to gain further insights into the magnetic order, we performed temperature-dependent neutron powder diffraction (NPD). The NPD data were collected on powder sample with weight of ~ 3 g using HB-2A Neutron powder diffractometer (NPDP) at Oak Ridge National Laboratory (ORNL), with Ge(113) monochromators giving wavelength 2.40 \AA ⁴⁶. The highest temperature due to experimental setup is 280 K, which below the T_N . The magnetic peak is determined through temperature dependent NPD data. As seen in the Figure 4a inset, when the temperature is decreased from 280 K down to 2 K, we observe an significant increase of the magnetic Bragg intensities on top of the nuclear Bragg

peaks. This suggests that the magnetic structure is resultant of a $k = (0,0,0)$ propagation vector which preserve the nuclear lattices translational symmetry. Figure 4a shows a diffraction pattern taken at 280 K along with Rietveld refinement results obtained using FULLPROF⁴². All Bragg peaks can be fit with the Rietveld refinement. The obtained refinement values $\chi^2 = 6.10$, $R_{\text{wp}} = 13.1$, and the R Bragg factor for the refinement of nuclear and magnetic phases are 4.278 and 17.55, respectively. There are three additional Bragg peaks at $Q \sim 2.7$, 3.1, and 4.4 \AA^{-1} , which belong to the aluminum sample holder and were added to the structural refinement as the minor phase. As the temperature is further decreased to 2 K, there is an increased intensity, centered at $Q \sim 1.4 \text{ \AA}^{-1}$, that is not described by the nuclear phase and likely originated from the magnetic phase.

To identify the magnetic structure, we further performed a full representational analysis for NPD data at 2 K to determine possible irreducible representations (irreps) and basis vectors (BVs) to describe the magnetic structure using the SARAh code⁴⁷. There is a total of 6 possible basis vectors corresponding to 6 irreps Γ_1 , Γ_3 , Γ_4 , Γ_6 , Γ_7 , Γ_8 . They are labeled following the scheme of SARAh and Kovalev⁴⁷ in Table SI in the Supplemental Material⁴⁸. Each irrep describes the magnetically distinct atoms within the unit cell. Within each irrep, each BV describes the possible direction of magnetic moments pointing along the a , b , and c -axis. We discriminated between all BVs by comparing the refinement values χ^2 and R factors and found that both Ψ_3 and Ψ_5 are required in order to obtain the best fit, as shown in Figure 4b. The Ψ_3 and Ψ_5 are from two different irreps implies that either there are two transitions or a strong first order transition. From the M - T plots presented in Figure 3a, only one transition was observed, therefore a first order transition seems more likely to be presented in BaFe_2Se_4 . The Ψ_5 indicates a ferromagnetic moment along the b -axis, while Ψ_3 suggests an antiferromagnetic moment along the a -axis, which further confirms the canted antiferromagnetic spin alignment in BaFe_2Se_4 . The obtained refinement values $\chi^2 = 6.82$ and $R_{\text{wp}} = 12.6$. The R Bragg factors for the refinement of nuclear and magnetic phases are 4.898 and 5.758, respectively.

The obtained magnetic structure of BaFe_2Se_4 can be described as Fe spins aligned perpendicular to the 1D molecular chains, antiferromagnetically correlated along the chain direction (the c -axis) as well as the interchain direction (the a -axis), with spins along the a -axis, and a small ferromagnetic canting along the b -axis, as shown in the inset of Figure 4b. The magnitude of the magnetic moment estimated from NPD data is $2.09 \mu_B/\text{Fe}$, with $1.98 \mu_B/\text{Fe}$ along the a -axis and $0.67 \mu_B/\text{Fe}$ along the b -axis. The magnetic moment canting angle is $\sim 18.7^\circ$ from the a -axis. Because of thermal fluctuations, a larger tilted angle of 63.1° is observed at 280 K comparing to 18.7° at 2 K. For comparison, in the tetrahedrally coordinated system, due to the crystal field effect, the magnetic moment of a free Fe^{3+} ion is $5.92 \mu_B$ for the high spin

state and $1.73 \mu_B$ for the low spin state taking the Lande factor $g = 2$. The calculated magnetic moment is in between the high spin and low spin state indicating a possible mixed state in this system. The magnitude of the magnetic moment is pretty close to that of single-chain quasi-1D TlFeSe_2 material with the same formal Fe^{3+} valence, but smaller than that of spin-ladder quasi-1D iron chalcogenide BaFe_2Se_3 with a formal Fe^{2+} valence. In TlFeSe_2 , the FeSe_4 tetrahedra also form a quasi-1D structure with Néel temperature at 295 K and the magnetic moment of Fe is $2.1 \mu_B/\text{Fe}$ ^{49–53}. The similar single 1D chain in both BaFe_2Se_4 and TlFeSe_2 , leads one to expect that both materials have similar direct and indi-

rect exchange interactions. However, the Dzyaloshinskii-Moriya interaction also arises, and this anisotropic exchange interaction leads to the canted antiferromagnetic ground state in the BaFe_2Se_4 . On the other hand, this canted antiferromagnetic structure in BaFe_2Se_4 is quite different from the typical magnetic structures discovered in spin-ladder quasi-1D iron chalcogenides, such as block-type structure in BaFe_2Se_3 , where four Fe spins along the chain form a Fe_4 ferromagnetic block, and each Fe_4 block stacks antiferromagnetically^{34,35}, or stripe-type structure in BaFe_2S_3 , KFe_2Se_3 and CsFe_2Se_3 , where Fe spins are ferromagnetic coupled along the rung direction and each ferromagnetic unit stacks antiferromagnetically along the leg direction^{36–38}.

The observation of the canted antiferromagnetism in this quasi-1D BaFe_2Se_4 compound is rather intriguing and could be a playground to further explore the correlations between magnetism and superconductivity. The antiferromagnetic order and/or magnetic spin fluctuations have been universally observed in the iron-based superconductors, and plays an important role for the emergence of superconductivity^{54–56}. BaFe_2Se_4 , with a simpler structure and higher symmetry than spin-ladder phase BaFe_2Se_3 , will provide a unique opportunity to reveal the intimate interplay between magnetism, crystal lattice and electronic structure in $[\text{FeX}_4]$ -based materials, and perhaps to understand the mechanism of superconductivity in Fe-based compounds. The BaFe_2Se_3 becomes superconducting at ~ 11 K at high pressure > 10 GPa. The appearance of superconductivity in BaFe_2Se_3 has a strong correlation with the magnitude of magnetic moments of Fe atoms, and the magnitude of magnetic moments is gradually decreasing with increasing pressure³⁹. It will be interesting to investigate how the magnetic structure and moment, canted antiferromagnetic correlation, and ferromagnetic component evolve with chemical doping or high pressure, whether superconductivity could be induced in the vicinity of this canted antiferromagnetism and how it interplays with the antiferromagnetism or even ferromagnetism when it emerges.

In summary, we have successfully synthesized high-quality polycrystalline sample of quasi-1D iron chalcogenide BaFe_2Se_4 . It has a semiconducting behavior with activation energy ~ 142 meV. Magnetic susceptibility measurements suggest a ferromagnetic-like transition at ~ 310 K, and NPD further reveals it is actually canted antiferromagnetism correlated along the 1D chain direction with a net small ferromagnetic moment in the perpendicular direction. The magnitude of the magnetic moment estimated from NPD data is $2.09 \mu_B/\text{Fe}$, which is pretty close to that of quasi-1D TlFeSe_2 material with the same Fe^{3+} valence, but smaller than that of other quasi-1D iron chalcogenides such as BaFe_2Se_3 with Fe^{2+} valence. This canted antiferromagnetic structure is also different from the typical block-type or stripe-type magnetism discovered in the quasi-1D iron chalcogenide such as BaFe_2Se_3 and BaFe_2S_3 , and could provide unique playground to study the interplay between magnetism,

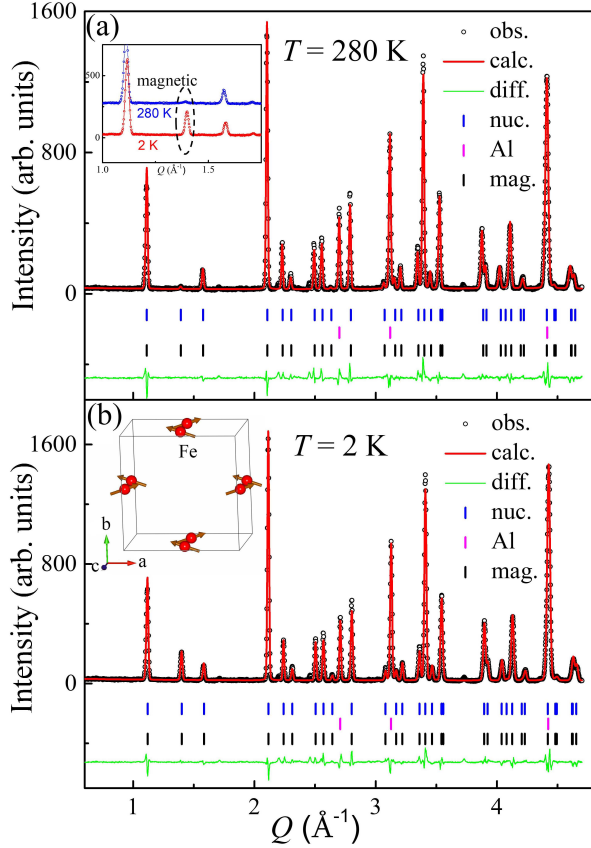


FIG. 4: (a) Rietveld refinement of neutron powder diffraction data of BaFe_2Se_4 at 280 K. The inset shows the increased intensity of magnetic peak when the temperature is decreased to 2 K. (b) Rietveld refinement of neutron powder diffraction data of BaFe_2Se_4 at 2 K. The black circles are experimental data and the red curve is the Rietveld refinement fit. The difference is shown at the bottom represented by the green curve. The positions of the nuclear and magnetic peaks of BaFe_2Se_4 and the peaks for the aluminum sample holder are marked by the blue, black, and magenta ticks, respectively. The inset shows the schematics of the magnetic structure of BaFe_2Se_4 (Red balls represent Fe atoms). The Fe spins are antiferromagnetically coupled along the chain direction (the c -axis) and the interchain direction (the a -axis), with spin along the a -axis, and a small ferromagnetic canting along the b -axis.

crystal lattice and electronic structure in the Fe-based compounds.

This work at University of Texas at Dallas is supported by US Air Force Office of Scientific Research (FA9550-19-1-0037), and National Science Foundation (DMR 1921581). We also acknowledge the support from

the Office of Research at University of Texas at Dallas through the Seed Program for Interdisciplinary Research (SPIRe) and the Core Facility Voucher Program. Support from Advanced Materials and Manufacturing Processes Institute (AMMPI) at the University of North Texas is acknowledged.

-
- * Electronic address: bly@utdallas.edu
- ¹ Y. Kamihara, H. Hiramatsu, M. Hirano, R. Kawamura, H. Yanagi, T. Kamiya, and H. Hosono, *J. Am. Chem. Soc.* **128**, 10012 (2006).
 - ² Y. Kamihara, T. Watanabe, M. Hirano, and H. Hosono, *J. Am. Chem. Soc.* **130**, 3296 (2008).
 - ³ F.-C. Hsu, J.-Y. Luo, K.-W. Yeh, T.-K. Chen, T.-W. Huang, P. M. Wu, Y.-C. Lee, Y.-L. Huang, Y.-Y. Chu, D.-C. Yan, et al., *PNAS* **105**, 14262 (2008).
 - ⁴ T. M. McQueen, Q. Huang, V. Ksenofontov, C. Felser, Q. Xu, H. Zandbergen, Y. S. Hor, J. Allred, A. J. Williams, D. Qu, et al., *Phys. Rev. B* **79**, 014522 (2009).
 - ⁵ Y. Mizuguchi, F. Tomioka, S. Tsuda, T. Yamaguchi, and Y. Takano, *Appl. Phys. Lett.* **93**, 152505 (2008).
 - ⁶ S. Margadonna, Y. Takabayashi, Y. Ohishi, Y. Mizuguchi, Y. Takano, T. Kagayama, T. Nakagawa, M. Takata, and K. Prassides, *Phys. Rev. B* **80**, 064506 (2009).
 - ⁷ S. Medvedev, T. M. McQueen, I. A. Troyan, T. Palasyuk, M. I. Erements, R. J. Cava, S. Naghavi, F. Casper, V. Ksenofontov, G. Wortmann, et al., *Nat. mater.* **8**, 630 (2009).
 - ⁸ D. Braithwaite, B. Salce, G. Lapertot, F. Bourdarot, C. Marin, D. Aoki, and M. Hanfland, *J. Phys.: Condens. Matter* **21**, 232202 (2009).
 - ⁹ G. Garbarino, A. Sow, P. Lejay, A. Sulpice, P. Toulemonde, M. Mezouar, and M. Núñez-Regueiro, *Europhys. Lett.* **86**, 27001 (2009).
 - ¹⁰ Q.-Y. Wang, Z. Li, W.-H. Zhang, Z.-C. Zhang, J.-S. Zhang, W. Li, H. Ding, Y.-B. Ou, P. Deng, K. Chang, et al., *Chin. Phys. Lett.* **29**, 037402 (2012).
 - ¹¹ D. Liu, W. Zhang, D. Mou, J. He, Y.-B. Ou, Q.-Y. Wang, Z. Li, L. Wang, L. Zhao, S. He, et al., *Nat. commun.* **3**, 1 (2012).
 - ¹² S. He, J. He, W. Zhang, L. Zhao, D. Liu, X. Liu, D. Mou, Y.-B. Ou, Q.-Y. Wang, Z. Li, et al., *Nat. mater.* **12**, 605 (2013).
 - ¹³ S. Tan, Y. Zhang, M. Xia, Z. Ye, F. Chen, X. Xie, R. Peng, D. Xu, Q. Fan, H. Xu, et al., *Nat. mater.* **12**, 634 (2013).
 - ¹⁴ J. J. Lee, F. T. Schmitt, R. G. Moore, S. Johnston, Y.-T. Cui, W. Li, M. Yi, Z. K. Liu, M. Hashimoto, Y. Zhang, et al., *Nature* **515**, 245 (2014).
 - ¹⁵ Z. Zhang, Y.-H. Wang, Q. Song, C. Liu, R. Peng, K. A. Moler, D. Feng, and Y. Wang, *Science bulletin* **60**, 1301 (2015).
 - ¹⁶ J. Guo, S. Jin, G. Wang, S. Wang, K. Zhu, T. Zhou, M. He, and X. Chen, *Phys. Rev. B* **82**, 180520 (2010).
 - ¹⁷ A. F. Wang, J. J. Ying, Y. J. Yan, R. H. Liu, X. G. Luo, Z. Y. Li, X. F. Wang, M. Zhang, G. J. Ye, P. Cheng, et al., *Phys. Rev. B* **83**, 060512 (2011).
 - ¹⁸ Y. Mizuguchi, H. Takeya, Y. Kawasaki, T. Ozaki, S. Tsuda, T. Yamaguchi, and Y. Takano, *Appl. Phys. Lett.* **98**, 042511 (2011).
 - ¹⁹ A. Krzton-Maziopa, Z. Shermadini, E. Pomjakushina, V. Pomjakushin, M. Bende, A. Amato, R. Khasanov, H. Luetkens, and K. Conder, *J. Phys.: Condens. Matter* **23**, 052203 (2011).
 - ²⁰ M.-H. Fang, H.-D. Wang, C.-H. Dong, Z.-J. Li, C.-M. Feng, J. Chen, and H. Q. Yuan, *Europhys. Lett.* **94**, 27009 (2011).
 - ²¹ T. Qian, X.-P. Wang, W.-C. Jin, P. Zhang, P. Richard, G. Xu, X. Dai, Z. Fang, J.-G. Guo, X.-L. Chen, et al., *Phys. Rev. Lett.* **106**, 187001 (2011).
 - ²² K. M. Taddei, M. Sturza, D.-Y. Chung, H. B. Cao, H. Claus, M. G. Kanatzidis, R. Osborn, S. Rosenkranz, and O. Chmaissem, *Phys. Rev. B* **92**, 094505 (2015).
 - ²³ M. Yi, D. H. Lu, R. Yu, S. C. Riggs, J.-H. Chu, B. Lv, Z. K. Liu, M. Lu, Y.-T. Cui, M. Hashimoto, et al., *Phys. Rev. Lett.* **110**, 067003 (2013).
 - ²⁴ M. Yi, Z.-K. Liu, Y. Zhang, R. Yu, J.-X. Zhu, J. J. Lee, R. G. Moore, F. T. Schmitt, W. Li, S. C. Riggs, et al., *Nat. Commun.* **6**, 1 (2015).
 - ²⁵ F. Ye, S. Chi, W. Bao, X. F. Wang, J. J. Ying, X. H. Chen, H. D. Wang, C. H. Dong, and M. Fang, *Phys. Rev. Lett.* **107**, 137003 (2011).
 - ²⁶ E. Dagotto, *Rev. Mod. Phys.* **85**, 849 (2013).
 - ²⁷ M. Burrard-Lucas, D. G. Free, S. J. Sedlmaier, J. D. Wright, S. J. Cassidy, Y. Hara, A. J. Corkett, T. Lancaster, P. J. Baker, S. J. Blundell, et al., *Nat. Mater.* **12**, 15 (2013).
 - ²⁸ X. F. Lu, N. Z. Wang, H. Wu, Y. P. Wu, D. Zhao, X. Z. Zeng, X. G. Luo, T. Wu, W. Bao, G. H. Zhang, et al., *Nat. Mater.* **14**, 325 (2015).
 - ²⁹ X. Dong, H. Zhou, H. Yang, J. Yuan, K. Jin, F. Zhou, D. Yuan, L. Wei, J. Li, X. Wang, et al., *J. Am. Chem. Soc.* **137**, 66 (2015).
 - ³⁰ X. Dong, K. Jin, D. Yuan, H. Zhou, J. Yuan, Y. Huang, W. Hua, J. Sun, P. Zheng, W. Hu, et al., *Phys. Rev. B* **92**, 064515 (2015).
 - ³¹ L. Zhao, A. Liang, D. Yuan, Y. Hu, D. Liu, J. Huang, S. He, B. Shen, Y. Xu, X. Liu, et al., *Nat. Commun.* **7**, 10608 (2016).
 - ³² Q. Liu, C. Chen, T. Zhang, R. Peng, Y.-J. Yan, C.-H.-P. Wen, X. Lou, Y.-L. Huang, J.-P. Tian, X.-L. Dong, et al., *Phys. Rev. X* **8**, 041056 (2018).
 - ³³ C. Chen, Q. Liu, T. Z. Zhang, D. Li, P. P. Shen, X. L. Dong, Z.-X. Zhao, T. Zhang, and D. L. Feng, *Chin. Phys. Lett.* **36**, 057403 (2019).
 - ³⁴ J. M. Caron, J. R. Neilson, D. C. Miller, A. Llobet, and T. M. McQueen, *Phys. Rev. B* **84**, 180409 (2011).
 - ³⁵ A. Krzton-Maziopa, E. Pomjakushina, V. Pomjakushin, D. Sheptyakov, D. Chernyshov, V. Svitlyk, and K. Conder, *J. Phys.: Condens. Matter* **23**, 402201 (2011).
 - ³⁶ S. Chi, Y. Uwatoko, H. Cao, Y. Hirata, K. Hashizume, T. Aoyama, and K. Ohgushi, *Phys. Rev. Lett.* **117**, 047003 (2016).
 - ³⁷ J. M. Caron, J. R. Neilson, D. C. Miller, K. Arpino, A. Llo-

- bet, and T. M. McQueen, Phys. Rev. B **85**, 180405 (2012).
- ³⁸ F. Du, K. Ohgushi, Y. Nambu, T. Kawakami, M. Avdeev, Y. Hirata, Y. Watanabe, T. J. Sato, and Y. Ueda, Phys. Rev. B **85**, 214436 (2012).
- ³⁹ J. Ying, H. Lei, C. Petrovic, Y. Xiao, and V. V. Struzhkin, Phys. Rev. B **95**, 241109 (2017).
- ⁴⁰ T. Yamauchi, Y. Hirata, Y. Ueda, and K. Ohgushi, Phys. Rev. Lett. **115**, 246402 (2015).
- ⁴¹ D. Berthebaud, O. Perez, J. Tobola, D. Pelloquin, and A. Maignan, J. Solid State Chem. **230**, 293 (2015).
- ⁴² J. Rodríguez-Carvajal, Physica B **192**, 55 (1993).
- ⁴³ B. H. Toby and R. B. Von Dreele, J. Appl. Cryst. **46**, 544 (2013).
- ⁴⁴ J. Gopalakrishnan and K. Nanjundaswamy, Bull. Mater. Sci. **5**, 287 (1983).
- ⁴⁵ H. Lei, H. Ryu, A. I. Frenkel, and C. Petrovic, Phys. Rev. B **84**, 214511 (2011).
- ⁴⁶ S. Calder, K. An, R. Boehler, C. R. Dela Cruz, M. D. Frontzek, M. Guthrie, B. Haberl, A. Huq, S. A. Kimber, J. Liu, et al., Rev. Sci. Instrum. **89**, 092701 (2018).
- ⁴⁷ A. S. Wills, Physica B **276**, 680 (2000).
- ⁴⁸ See Supplemental Material for Canted Antiferromagnetism in the Quasi-1D Iron Chalcogenide BaFe_2Se_4 .
- ⁴⁹ Z. Seidov, H.-A. Krug von Nidda, J. Hemberger, A. Loidl, G. Sultanov, E. Kerimova, and A. Panfilov, Phys. Rev. B **65**, 014433 (2001).
- ⁵⁰ E. B. Asgerov, N. T. Dang, A. I. Beskrovnyy, A. I. Madadzada, D. I. Ismayilov, R. N. Mehdiyeva, S. H. Jabarov, and E. M. Karimova, Semiconductors **49**, 879 (2015).
- ⁵¹ N. A. Ismayilova, H. S. Orudjev, and S. H. Jabarov, Semiconductors **51**, 473 (2017).
- ⁵² Z. Seidov, H.-A. Krug von Nidda, V. Tsurkan, I. Filippova, A. Günther, A. Najafov, M. N. Aliyev, F. G. Vagizov, A. G. Kiiamov, L. R. Tagirov, et al., Bull. Russ. Acad. Sci.: Phys. **81**, 885 (2017).
- ⁵³ E. B. Asgerov, D. I. Ismayilov, R. N. Mehdiyeva, S. H. Jabarov, M. N. Mirzayev, E. M. Kerimova, and N. T. Dang, J. Surf. Invest.: X-Ray, Synchrotron Neutron Tech. **12**, 688 (2018).
- ⁵⁴ J. M. Allred, K. M. Taddei, D. E. Bugaris, M. J. Krogstad, S. H. Lapidus, D. Y. Chung, H. Claus, M. G. Kanatzidis, D. E. Brown, J. Kang, et al., Nat. Phys. **12**, 493 (2016).
- ⁵⁵ D. N. Basov and A. V. Chubukov, Nat. Phys. **7**, 272 (2011).
- ⁵⁶ R. M. Fernandes and A. V. Chubukov, Rep. Prog. Phys. **80**, 014503 (2016).

Supplemental Material for ‘Canted Antiferromagnetism in the Quasi-1D Iron Chalcogenide BaFe₂Se₄’

Xiaoyuan Liu,¹ Keith M. Taddei,² Sheng Li,¹ Wenhao Liu,¹ Nikhil Dhale,¹

Rashad Kadado,¹ Diana Berman,³ Clarina Dela Cruz,² and Bing Lv^{1,4}

¹*Department of Physics, University of Texas at Dallas, Richardson, Texas 75080, USA*

²*Neutron Scattering Division, Oak Ridge National Laboratory, Oak Ridge, Tennessee 37831, USA*

³*Department of Materials Science and Engineering,
University of North Texas, Denton, Texas 76203, USA*

⁴*Department of Materials Science and Engineering,
University of Texas at Dallas, Richardson, Texas 75080, USA*

Table SI: Basis vectors (BVs) of irreducible representations (irreps) for the space group $I4/m$ with the magnetic propagation vector $k = (0, 0, 0)$

Irreps	BVs	Basis vector components			
Γ_i	Ψ_i	Atoms	m_a	m_b	m_c
Γ_1	Ψ_1	Fe1	0	0	4
		Fe2	0	0	4
Γ_3	Ψ_2	Fe1	4	0	0
		Fe2	4	0	0
Γ_4	Ψ_3	Fe1	4	0	0
		Fe2	-4	0	0
Γ_6	Ψ_4	Fe1	0	0	4
		Fe2	0	0	-4
Γ_7	Ψ_5	Fe1	0	-4	0
		Fe2	0	-4	0
Γ_8	Ψ_6	Fe1	0	4	0
		Fe2	0	-4	0